Supporting Materials for:

High Spatiotemporal-Resolution Magnetic Tweezers: Calibration and Applications for DNA Dynamics

David Dulin,[1,*], Tao Ju Cui,[1] Jelmer Cnossen,[1] Margreet W. Docter,[1] Jan Lipfert,[2] and Nynke H. Dekker[1,*]

[1]Department of Bionanoscience, Kavli Institute of Nanoscience, Delft University of Technology, Delft, The Netherlands; and [2]Department of Physics, Nanosystems Initiative Munich and Center for Nanoscience, Ludwig-Maximilians-University Munich, Munich, Germany

*To whom the correspondence maybe addressed: daviddulin82@gmail.com or n.h.dekker@tudelft.nl

This document contains Supplementary Text and 5 Supplementary Figures.

Supplementary Text

Spatiotemporal resolution for surface-melted beads as a function of illumination intensity and bead size

As discussed in the main text, the light intensity available for sample illumination is a factor that must be carefully considered in high-speed video tracking. At low light intensities, the tracking noise will become the limiting factor; conversely, at saturating illumination intensities, the lack of contrast between the rings in the diffraction pattern will become limiting. Here, we characterize the achievable spatiotemporal resolution as a function of the illumination light intensity (**Fig. S3**) prior to testing the optimal configuration (**Fig. 2B**).

To quantify the light intensity in the field of view, we average the discrete grey levels of the camera (8 bits, corresponding to 256 grey levels) over the entire field of view. We observe a significant increase in resolution for light illumination intensities that yield a camera response up to 200 grey levels (**Fig. S3A-F**). However, the improvement in the resolution of bead positions levels off for light intensities exceeding 150 grey levels; we achieve an optimal resolution of 0.014 nm at 4 s using 175 grey levels for a trace acquired at 500 Hz under LED illumination (**Fig. S3C,F**). This same trend is observed for beads of different types: MyOne magnetic beads (1 μm diameter, **Fig. S3A**), small latex beads (1.5 μm diameter, **Fig. S3B**), M270 beads

(2.8 μm diameter, **Fig. S3C**), and large latex beads (3 μm diameter, **Fig. S3D**): spatial resolution always improves with increased illumination intensity (until 200 grey levels, **Fig. S3E**) and with longer averaging times τ, until drift becomes limiting at τ ~1-10 s.

We also evaluate how the achievable spatial resolution differs for these types of surface-melted beads (**Fig. S3**). First, we observe that a bead's material composition (magnetic vs. latex) does not impact the achievable resolution (**Fig. S3F**, compare polystyrene beads in red and magnetic beads in blue). However, we do see a two-fold improvement in spatial resolution when we use larger beads (dashed lines for smaller beads, plain lines for larger beads, **Fig. S3F**). For example, in the case of M270 beads (solid blue line, **Fig. S3F**), the Allan deviation (AD) equals 0.1 nm and 0.02 nm over time intervals of 0.01 s and 1 s, respectively, while in the case of MyOne beads, the AD is limited to 0.4 nm and 0.04 nm over the same time intervals (dashed blue line, **Fig. S3F**). This result is in agreement with the recent work of Seidel and co-workers (29) in which they observed an improvement of the spatiotemporal resolution using larger beads and a reduction in AD with the averaging temporal window, following a power law in $1/\sqrt{N}$, identically to our results. We represent the Allan deviation for a given time interval (0.13 s) from **Fig. S3F** as a function of the bead size (blue circle, **Fig. S3G**) and we observed that the AD decreases as $1/R_{bead}$ (black solid line, **Fig. S3G**). This observation is consistent with a scattered light intensity described by the Mie theory ($I_{scatt} \propto 1/R_{bead}^2$), which is valid for a sphere with a radius larger than the wavelength of the illumination light, and an AD following a power law of the form $1/\sqrt{I}$ (solid red line, **Fig. S3E**). If the scattered light intensity was described by the Rayleigh theory (valid for sub-wavelength radius objects), the AD would have decayed as $1/R_{bead}^3$ (black dashed line, Fig. S3G), which does not fit our experimental results.

Spatiotemporal resolution of a dsDNA or a ssDNA tethered beads determined from numerical simulation.

We simulate the fluctuations z-axis of a magnetic bead of 1 μm diameter tethered to a 1.9 kbp DNA, and experiencing a force of 18 pN (**Fig. S4**) (43). We simulated traces

for duration of 3 s, sampled at 0.1 μs, subsequently boxcar-filtered at either 8 kHz or 500 Hz to simulate the camera shutter time used in our experiments. We first perform simulations in the absence of tracking noise: in this case, theory predicts (Eq. 3) that traces acquired at different acquisition frequencies should display identical values of the AD for a given time window. This prediction is confirmed by our numerical simulations: the AD of box-car filtered traces acquired at 8 kHz (dashed pink line, **Fig. S4A**) and 500 Hz (solid pink line, **Fig. S4A**) are identical. Next, we add Gaussian noise with a standard deviation of 1 nm to these simulated traces to mimic the tracking noise on a 1 μm diameter magnetic bead (**Fig. S3A-F**). A comparison of two simulated traces at 8 kHz in the absence (dashed pink line, **Fig. S4B**) and presence of noise (dashed purple line, **Fig. S4B**) shows how the AD increases in the presence of tracking noise, as it should since the total noise is the quadratic sum of the thermal noise and the tracking noise. Lastly, we compare simulated traces with tracking noise at the two different acquisition frequencies, 8 kHz (dashed purple line, **Fig. S4C**) and 500 Hz (solid purple line, **Fig. S4C**). The trace simulated at 8 kHz displays a clear improvement in the magnitude of the AD, as the tracking noise is averaged as $1/\sqrt{N}$ (**Fig. S3F**).

Similarly to the dsDNA-tethered bead, we simulate the fluctuations along the z-axis for the case of an open hairpin, e.g. a ssDNA-tethered bead. In short, we simulate a 1 μm diameter magnetic bead tethered to a 2 kb ssDNA under a force of 19 pN (**Fig. S4**). The simulated traces are sampled at 1 μs for a duration of 10 s, and subsequently boxcar-filtered at either 8 kHz or 500 Hz to simulate the camera shutter time employed. As above, the numerical simulations show that the AD of traces box-car filtered at either 8 kHz (dashed green line, **Fig. S4A**) or 500 Hz (solid green line, **Fig. S5B**) are identical for a given time window. Adding Gaussian noise of 1 nm standard deviation to the simulated traces at 8 kHz and 500 Hz, we observe no change in ADs (**Fig. S5B-C**), confirming what we observed experimentally in **Fig. 3D**, meaning that the resolution is limited by the thermal noise. In that case, a faster acquisition rate does not provide a better spatiotemporal resolution.

Spatiotemporal resolution for DNA-hairpin tethered beads as a function of bead size and tether length

In the main text, we discuss the spatiotemporal resolution of dsDNA- and hairpin-tethered beads. For both types of tethers, considerations of the bead radius and the tether length and nature (Eqs. 2,3 of the main text) need to be taken into account. As an example, we here consider the bead-size and tether-length considerations for hairpin-tethered beads (**Fig. 1A**).

Generally speaking, temporal resolution for a tethered bead is expected to improve with smaller beads and shorter tethers, as can be deduced from Eq. 5 of the main text, which indicates that the bandwidth of the system scales with these two parameters. As a consequence, providing a tether-bead system with a larger bandwidth offers the possibility to observe fast enzymatic steps. However, when using a smaller magnetic bead, it is important to not be limited by the loss in tracking accuracy.

To test the effect of the bead size on the spatiotemporal resolution, we compare the thermal noise for beads of different diameters (1 μm diameter MyOne beads, black lines in **Fig. S5E**; 2.8 μm diameter M270 beads; grey lines in **Fig. S5E**) located ~200 nm away from the flow chamber surface (**Fig. 1A**) via hairpin tethering (**Fig. 1A**). As in the main text, the comparison is performed by computing the respective AD along the *z* axis. For M270 beads, we acquire data at 2 kHz with a high-power fiber-coupled LED illumination, whereas for MyOne beads, we acquire data at 4 kHz using laser-based illumination (**Fig. S5A**). For both bead types, we first compare the noise for closed hairpins (force ~12 pN, solid lines in **Fig. S5E**). We observe that the AD peak is shifted to shorter timescales for MyOne beads (black solid lines, **Fig. S5E**) compared to M270 beads (grey solid lines, **Fig. S5B**), with corresponding peak amplitudes of ~2 nm at ~0.25 ms and ~3 nm at ~3 ms, respectively. Given that the hairpin handle is predominantly composed of dsDNA, we initially model these tethers as double-stranded nucleic acids with an extension of 200 nm (and a persistence length L_P of 50 nm). For both bead types, theory predicts peak amplitudes of 1.2 nm that are comparable to experimental observations; however, it also predicts timescales of 0.023 and 0.26 ms, respectively, th at are found to be ten-fold shorter than experimentally observed. To understand this discrepancy in timescales, we revise the modeling, assuming that the handles perform mechanically as if they predominantly consisted of ssDNA (with $L_P = 0.5$ nm). In doing so, we obtain much better agreement with the experimental results (predicted peak amplitudes of 2.7 nm for

both bead types, with timescales of 0.12 ms and 1.3 ms, respectively). This result implies that the single-stranded portions of the handles dominate the dynamics of our bead-closed hairpin system. On longer timescales, we note that the AD continues to decrease until drift starts to dominate at $\tau > 1$ s (**Fig. S5E**) (31, 46) for both bead types. At the local minimum of the AD, we measure amplitudes of ~ 0.3 nm for MyOne beads and ~ 0.6 nm for M270 beads. These values exceed theoretical predictions (under the assumption of predominantly ssDNA handles) by factors of 8 and 4, respectively. This increased noise observed experimentally may result from hairpin dynamics, e.g. slow partial fraying and reannealing of the hairpin, that dominate the noise on longer timescales.

Using a smaller bead provides a smaller correlation time for a similar AD peak amplitude, hence the spatiotemporal resolution is improved for an equivalent time averaging window (Eq. 3 in the main text) larger than the correlation time of the system (**Fig. S5E**).

We have also examined the spatiotemporal response of different bead types that are tethered to open hairpins (force ~19 pN, $k_z \sim 0.55\ pN/nm$, dashed lines in **Fig. S5E**). We measure that the peak of the AD for M270 beads lies at ~1 ms (grey dashed line, **Fig. S5E**), whereas it lies at ~0.25 ms for MyOne beads (black dashed line, **Fig. S5E**; with some uncertainly as it is difficult to accurately determine the peak position here), with an amplitude of ~ 4 nm for both beads. Our model (assuming a ssDNA extension of 1 μm), predicts peak amplitudes of 6 nm located at 0.25 ms for MyOne beads and at 1.8 ms for M270 beads, in good agreement with the experimental results. On longer timescales (~1 s), the experimentally measured peak AD amplitudes of ~ 0.2 nm for MyOne beads and ~ 0.3 nm for M270 beads match up well with theoretical predictions (0.14 nm for MyOne beads; 0.37 nm for M270 beads). Thus, the gain in bandwidth by using smaller beads with open hairpins provides an improved spatiotemporal resolution, as in the case of beads tethered to closed hairpins. These results confirm the prediction that one should employ the smallest possible beads to maximize the information that can be extracted at short timescales (6), as this allows one to attain, upon averaging to a lower bandwidth, increased spatiotemporal resolution. We note in particular that this result is, independent of whether a bead is tethered to a closed or open hairpin. The agreement between theory

and experiment furthermore highlight how the simple model that we introduce can be successfully employed to evaluate the spatiotemporal response for a tethered molecule. This can be useful to experimentalists as it allows one to design experimental conditions in order to observe catalytic activity at optimal resolution.

Lastly, we investigate the effect of tether length on the spatiotemporal resolution achievable with DNA hairpins, where we expect that the use of a short, and therefore stiff construct (**Fig. 1B**), will provide the best spatiotemporal resolution (Eq. (2) in the main text) when using the same type of bead. We compare the AD for closed hairpins with ~200 nm and ~700 nm handles, respectively. For both cases, we employ 1 μm diameter MyOne beads and laser illumination. The AD of the hairpin with the 700 nm handle peaks at ~0.4 ms with a magnitude of ~5 nm (**Fig. S5F**, black arrows), which compares well to the theoretically computed values of 0.2 ms and 5 nm (ssDNA handles, Eqs. 3, 5 of the main text). As expected, the hairpin with the 200 nm handle provides improved spatiotemporal resolution, with an AD that peaks at ~0.25 ms with a magnitude of ~2 nm (**Fig. S5F,** solid blue line). Over a time interval of 1 s, we measure an AD of 0.3 nm at 1 s for the hairpin with the ~200 nm handle (**Fig. S5F**, blue solid line), which is a three-fold improvement over the AD of 0.9 nm for the hairpin with the ~200 nm handle (**Fig. S5F**, blue dashed line). However, on this timescale the experimentally measured values are tenfold higher than theoretical predictions, which yield 0.1 nm (0.04 nm) for the hairpin with the longer (shorter) handle. The origin of the discrepancy is likely common to both two hairpins and may derive from slow hairpin dynamics, as described above. From these results, we conclude that the gain in noise reduction and bandwidth through the use of a shorter (hence stiffer) molecule exceeds any reductions in bandwidth that result from the increased friction associated with surface proximity, as predicted by theory (Eqs. 3, 5, 6 of the main text, **Fig. 1B**).

Oligonucleotides involved in the hairpin design of Figure S1 (polarity: 5'->3')

1-kb fragment:

CTCCTGTGTGGTCTCGTTGCGAAGTAGTTATTAGCCACCCAGGAACCAAAAAAAAAA
AAAAAAAAAAAAAAAAAAAAAAAAAAAAAAAAAAAAAAAAAAAAAAAAAAAAAAAA
AAAAAAAAAAAAAAAAAAAAAAAAAAAAAAAAAAAAAAAAAAAAAAAAAAAAAAAA

AAAAAAAAAAAAAAAAAAAACTCGAGGAGCTTGGCACTGGCCGTCGTTTTACAACGT
CGTGACTGGGAAAACCCTGGCGTTACCCAACTTAATCGCCTTGCAGCACATCCCCCTT
TCGCCAGCTGGCGTAATAGCGAAGAGGCCCGCACCGATCGCCCTTCCCAACAGTTGCG
CAGCCTGAATGGCGAATGGCGCCTGATGCGGTATTTTCTCCTTACGCATCTGTGCGGT
ATTTCACACCGCATATGGTGCACTCTCAGTACAATCTGCTCTGATGCCGCATAGTTAA
GCCAGCCCCGACACCCGCCAACACCCGCTGACGCGCCCTGACGGGCTTGTCTGCTCCC
GGCATCCGCTTACAGACAAGCTGTGACCGTCTCCGGGAGCTGCATGTGTCAGAGGTT
TTCACCGTCATCACCGAAACGCGCGAGACGAAAGGGCCTCGTGATACGCCTATTTTTA
TAGGTTAATGTCATGATAATAATGGTTTCTTAGACGTCAGGTGGCACTTTTCGGGGA
AATGTGCGCGGAACCCCTATTTGTTTATTTTTCTAAATACATTCAAATATGTATCCG
CTCATGAGACAATAACCCTGATAAATGCTTCAATAATATTGAAAAAGGAAGAGTATG
AGTATTCAACATTTCCGTGTCGCCCTTATTCCCTTTTTTGCGGCATTTTGCCTTCCTG
TTTTTGCTCACCCAGAAACGCTGGTGAAAGTAAAAGATGCTGAAGATCAGTTGGGTG
CACGAGTGGGTTACATCGAACTGGATCTCAACAGCGGTAAGATCCTTGAGAGTTTTC
GCCCCGAAGAACGTTTTCCAATGATGAGCACTTTTAAAGTTCTCCTAGGAGACCCGG
TATTATC

Primer 1458:
GGCCAACCAAGTCATTCTGAGAATAGTGTATGCGGCGACCGAGTTGCTCTTGCCTTT
TTTTTTTATGCTCTTTACAACCGGTTGACTGCTTCAGGGGTCGATCCCGCTTTGTAC
Primer 1459:
GCAAGTACAAAGCGGGATCGACCCCTGAAGCAGTCAACCGGTTGTAAAGAGCATGCC
AGATGGTAAGCCCTCCCGTATCGTAGTTATCTACACGACGGGGAGTCAGGCAACTAT
GGATGAACGA
Primer 1460:
GATCTCGTTCATCCATAGTTGCCTGACTCCCCGTCGTGTAGATAACTACGATACGGGA
GGGCTTACCATCTGGC
Primer 1461:
ATTCTCAGAATGACTTGGTT
Primer 1462:
GAGCAACTCGGTCGCCGCATACACTATTCTCAGAATGACTTGGTT
Primer 1531:
CCTAAGCTCGCCGAGGCGAGCGAAAGCTCGCCTCGGCGAGCT

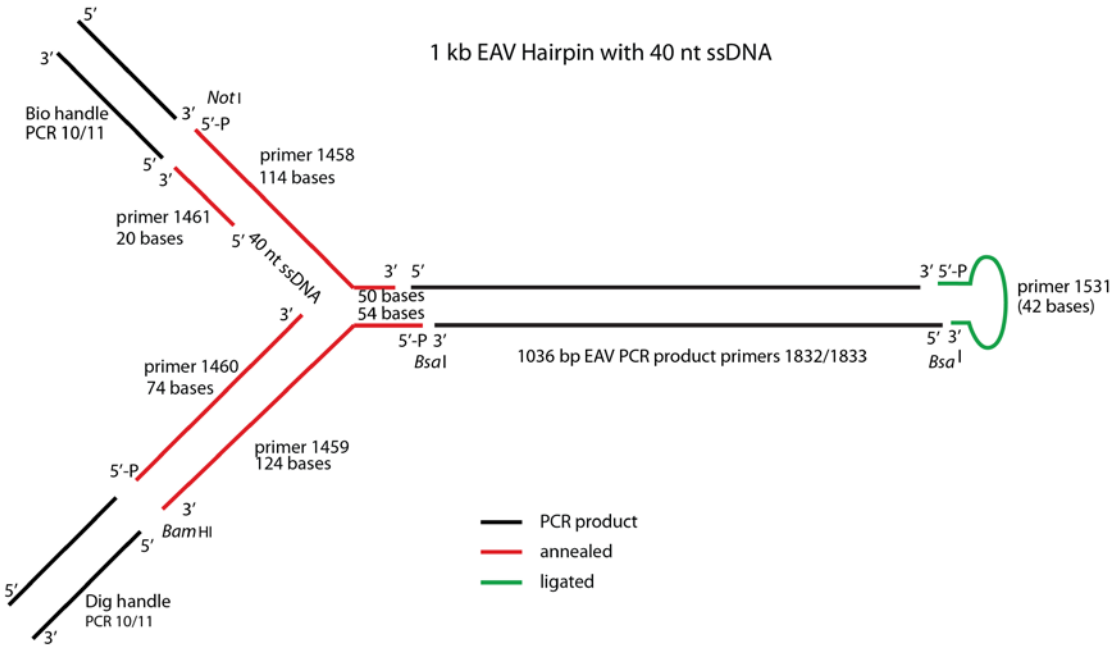

Figure S1: Hairpin design described in the Materials and Methods of the main text and used for the studies detailed in Figures 3, 4, 5.

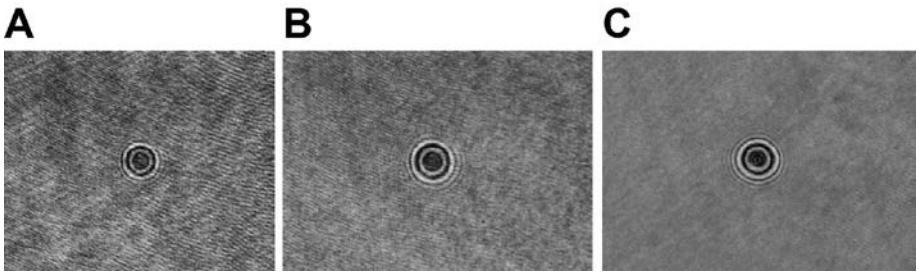

Figure S2: Field of view with a surface-melted M270 magnetic bead in different conditions of laser-based illumination: Without fast modulation and without per-pixel linear correction (**Materials and Methods**) **(A)**, With fast modulation and without per-pixel linear correction **(B)**, With fast modulation and with per-pixel linear correction **(C)**.

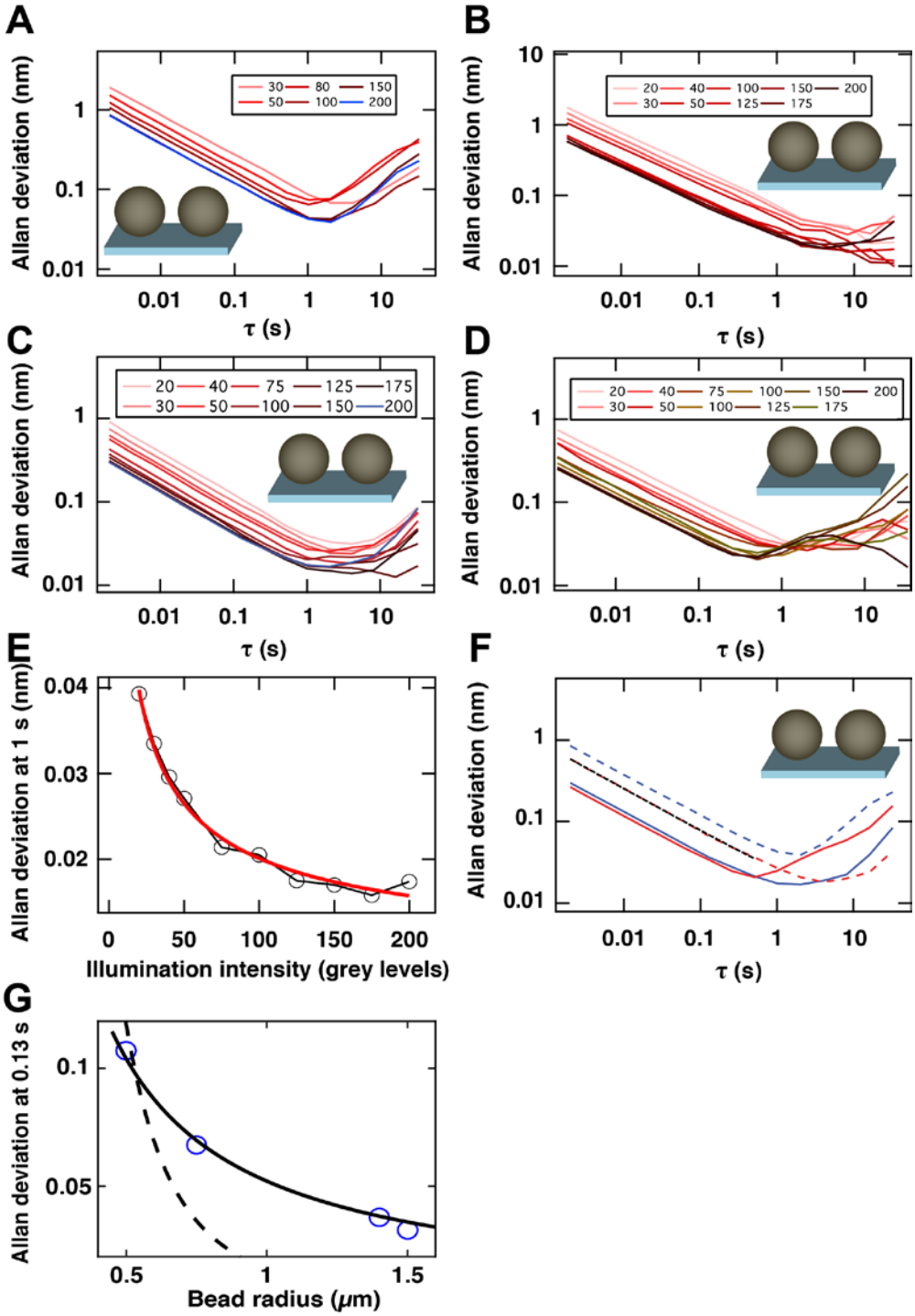

Figure S3: Allan deviation along the z-axis for different types of surface melted beads and illumination intensities. (A) A 1 μm diameter MyOne magnetic bead. **(B)** 1.5 μm diameter polystyrene bead. **(C)** A 2.8 μm diameter M270 beads. **(D)** A 3 μm diameter polystyrene bead. For τ>1 s, we observed an increase in the values of the AD. This increase in the AD values results from a lower statistics at large τ, which depends on the duration of the measurement. **(E)** The Allan deviation measured in (B) at 1 s is represented as a function of the light intensity on the camera (grey levels). The red line is a fit to the Allan deviation at 1s to a power law of the form $A \cdot I^x$, yielding $x = -0.55 \pm 0.13$, I being the average intensity on the camera. **(F)** Comparison of the Allan deviations for different types of surface-melted beads and 200 grey levels:

Myone beads (1 μm diameter, blue dashed line); small latex beads (1.5 μm diameter, red dashed line); M270 beads (2.8 μm diameter, blue solid line); and large latex beads (3 μm diameter, red solid line). Black dashed line: fit to the data for the small latex bead to a power law of the form $A \cdot \tau^x$, yielding $x = -0.52 \pm 0.05$. To acquire these datasets, we employ high-power LED illumination and perform real-time tracking at an acquisition frequency of 500 Hz. In all cases, the position of the tracked bead is corrected for drift via reference bead subtraction (**Fig. 1A**). **(G)** The Allan deviation measured at 0.13 s in (F) is represented as a function of the bead radius (blue circle). The black solid line and the black dashed line are fits of the form $1/R_{bead}$ and $1/R_{bead}^3$, respectively.

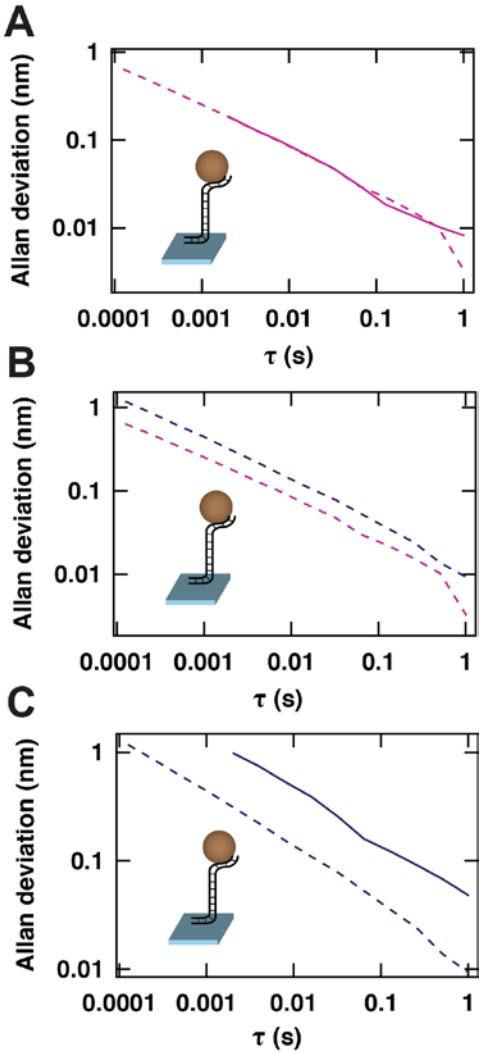

Figure S4: Numerical simulations to determine the resolution along the z-axis for a tethered magnetic bead when the noise is dominated by the tracking noise. From a numerical simulation of the motion of a 1 µm diameter magnetic bead tethered to a 1.9 kbp long dsDNA experiencing a force of 18 pN (simulation total duration: 5 s; sampling time: 0.1 µs), we compare: **(A)** the Allan deviation of the z-position for a boxcar-filtered 8 kHz trace (dashed pink line) and a boxcar-filtered 500 Hz (solid pink line); **(B)** the Allan deviation of the z-position for a boxcar-filtered 8 kHz trace (dashed pink line) and the same trace including an additional gaussian noise of 1 nm standard deviation to simulate the tracking noise (dashed purple line); **(C)** the Allan deviation of the z-position for a boxcar-filtered 8 kHz trace (dashed purple line) and a boxcar-filtered 500 Hz (solid purple line), both including an additional a gaussian noise of 1 nm standard deviation to simulate the tracking noise.

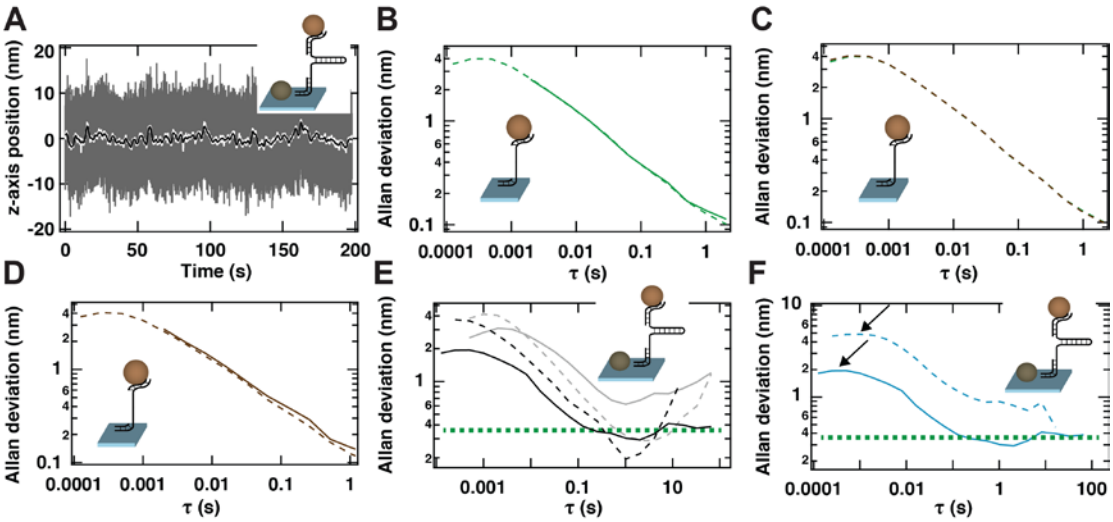

Figure S5: Experiments and numerical simulations to determine the resolution along the z-axis for a tethered magnetic bead when the noise is dominated by the thermal noise. (A) Typical trace of the tracked position along the *z*-coordinate of MyOne magnetic bead tether on a DNA hairpin with an applied force of ~12 pN. We use a laser-based illumination, the number of grey levels is set to 150, and real-time tracking is performed at 4 kHz simultaneously for the tethered bead and a surface-melted reference bead, whose position along the *z*-axis has been subtracted. Grey line: raw data, white line: box-car filtered 10 Hz, black line: box-car filtered 1Hz. From a numerical simulation of the motion of a 1 μm diameter magnetic bead tethered to a 2 kb long ssDNA experiencing a force of 19 pN (simulation total duration: 3 s; sampling time: 0.1 μs), we compare: **(B)** the Allan deviation of the z-position for a boxcar-filtered 8 kHz trace (dashed green line) and a boxcar-filtered 500 Hz (solid green line); **(C)** the Allan deviation of the z-position for a boxcar-filtered 8 kHz trace (dashed green line) and the same trace including an additional gaussian noise of 1 nm standard deviation to simulate the tracking noise (dashed brown line); **(D)** the Allan deviation of the z-position for a boxcar-filtered 8 kHz trace (dashed brown line) and a boxcar-filtered 500 Hz (solid brown line), both including an additional gaussian noise of 1 nm standard deviation to simulate the tracking noise. **(E)** The Allan deviation of the *z*-position for DNA hairpin-tethered MyOne (black dashed and solid lines) and M270 (grey dashed and solid lines) beads. The reference bead position has been subtracted from that of the hairpin-tethered beads prior to computation of the Allan deviation. Illumination is provided by a high power fiber-coupled LED for the M270 beads and using laser illumination for the MyOne beads, the number of grey levels is set to 150, real-time tracking is performed at 2 kHz for M270 beads and at 4 kHz for MyOne beads, and the applied force equals either ~19 pN (open hairpin, dashed lines) or ~12 pN (closed hairpin, solid lines) **(F)** The Allan deviation of the *z*-position of dsDNA hairpin-tethered MyOne beads, where the length of the tether handles is either ~200 nm (blue solid line) or ~700 nm (blue dashed line), with both beads position corrected by subtracting a reference bead position. Illumination is provided by a laser, the number of grey levels is set to 150, real-time tracking is performed at 8 kHz for the tethers with short handles and at 4 kHz for the tethers with long handles, and the applied force equals ~12 pN (closed hairpin).

The arrows indicate the positions of the peak position of the AD of the bead-DNA hairpin system.